AMS Home   Journals Home   Journal Archive   Subscribe   For Authors   Help   Advanced Search   Search   Go

Full Text View

Evolution of Mean-Flow Fofonoff Gyres in Barotropic Quasigeostrophic Turbulence

John K. Dukowicz

Theoretical Division, Los Alamos National Laboratory, Los Alamos, New Mexico

Richard J. Greatbatch

Department of Oceanography, Dalhousie University, Halifax, Nova Scotia, Canada

ABSTRACT

Numerical experiments are performed over a wide range of parameters to show that mean flows in the form of Fofonoff gyres, characterized by a linear relationship between streamfunction and potential vorticity, are universally produced in the statistically steady state of inviscid unforced barotropic quasigeostrophic turbulence, provided that the initial state is sufficiently well resolved. Further, as the resolution is increased, the mean-flow energy approaches the total energy, and the mean-flow potential enstrophy reaches a minimum value, which is lower than the value with no flow. This is in agreement with the predictions of the theory of equilibrium statistical mechanics. The timescale for the appearance of these flows is on the order of 5–$10\tau_E$, where τ_E is a mean eddy turnover time. When viscosity is turned on, the mean-flow Fofonoff gyres become internally homogenized and eventually disappear entirely as the flow decays to zero. This evolution of the gyres can be universally scaled with a timescale $\tau_v = \delta^2/v,$ where δ is the Rhines scale and v is the viscosity coefficient. There is an initial period of very rapid adjustment on a timescale of $\sim 0.005\tau_v$ at the enstrophy accumulated at very high wavenumbers is dissipated, followed by an intermediate period with a timescale of $\sim 0.04\tau_v$ during which the gyres are homogenized, and finally a period of gyre decay on a timescale of $\sim 0.3\tau_v$. In general, there is a competition between the statistical tendency to organize the mean flow into Fofonoff gyres

Options:
- Create Reference
- Email this Article
- Add to MyArchive
- Search AMS Glossary

Search CrossRef for:
- Articles Citing This Article

Search Google Scholar for:
- John K. Dukowicz
- Richard J. Greatbatch

and the tendency for homogenization, with the tendency to form Fofonoff gyres being always overwhelmed given a sufficiently long time. Thus, the issue of whether statistical mean flows, such as Fofonoff gyres, emerge and play a role depends on the relative magnitude of the two timescales, τ_E and τ_v.

1. Introduction

The study of geostrophic turbulence, while important in its own right, is also necessary for the practical reason that computer models of the atmosphere and the oceans are generally unable to resolve turbulence scales and therefore require accurate and reliable turbulence parameterizations. One common starting point of interest to both meteorology and oceanography is the quasigeostrophic barotropic flow in a single layer of nonuniform thickness, given by the equation for the advection of potential vorticity:

$$\frac{dq}{dt} = \partial_t q + \mathbf{u} \cdot \nabla q = 0, \qquad (1)$$

where the velocity $\mathbf{u} = (-\partial_y \psi, \partial_x \psi)$ is given in terms of the streamfunction ψ. The potential vorticity is $q = \zeta + f + h^*$, where

$$\zeta = \nabla^2 \psi \qquad (2)$$

is the relative vorticity, f is the Coriolis parameter, and h^* is a topographical function directly related to the thickness of the layer. In this paper, however, we will confine ourselves to perhaps the simplest case, namely, that of a constant thickness layer on a β plane, in which case, $q = \zeta + \beta y$, where y is the coordinate in the meridional direction, and $\beta = \partial_y f$. In this case, (1) may be written as

$$\partial_t \zeta + J(\psi, q) = 0, \qquad (3)$$

where the Jacobian is given by $J(\psi, q) = \partial_x \psi \, \partial_y q - \partial_y \psi \, \partial_x q$. This, together with the definition of ζ in (2), is a single scalar equation for ψ, with the boundary condition $\psi = 0$. Note that by omitting topography we have not lost anything essential since topography acts analogously to rotation in the definition of potential vorticity, and therefore the βy term is in effect a simplified topographic term.

If we omit $f + h^*$ or βy from the definition of q in (1) or (3), respectively, then we recover standard inviscid incompressible two-dimensional flow, and therefore quasigeostrophic turbulence in this simple setting shares many of the properties of conventional two-dimensional turbulence (Bretherton and Haidvogel 1976). In particular, they both possess a dual cascade: a direct cascade of enstrophy to smaller scales and an inverse cascade of energy to larger scales when forced or when starting from an initial condition at intermediate scales. In addition, they share the remarkable property that volume in the phase space of independent degrees of freedom (e.g., Fourier modes) is conserved, making it possible to apply the methods of statistical mechanics to the problem. The exploitation of this fact dates back to Onsager (1949) for the case of two-dimensional turbulence and to Salmon et al. (1976) for the case of quasigeostrophic turbulence. For a review of geostrophic turbulence see Rhines (1979), and of the associated statistical mechanics see Holloway (1986).

Equilibrium statistical mechanics makes it possible to predict the mean flow in the statistical steady state of unforced inviscid turbulence. The theory states that the mean potential vorticity is a linear function of the mean streamfunction:

$$\langle q \rangle = \mu \langle \psi \rangle + \lambda, \qquad (4)$$

where the angle brackets denote ensemble or time averages and μ and λ are constants. In the oceanic case on a β plane, (4) implies the formation of Fofonoff gyres (Fofonoff 1954) inside a bounded domain. For the meridionally symmetric experiments considered in this paper, the parameter $\lambda = 0$, and the flow consists of a pair of Fofonoff gyres with a central broad westward jet and relatively narrow return currents on the boundaries. In other words, statistical mechanics predicts that unforced turbulence associated with Eq. (3) will spontaneously organize itself into a mean flow given by Fofonoff gyres, and this will persist indefinitely. A detailed discussion of such a state is given by Carnevale and Frederiksen (1987).

The prediction of Fofonoff gyres and related topographically induced mean flows is unique to geostrophic turbulence. Holloway has named this the "Neptune effect" and has long advocated its incorporation into turbulence parameterizations for

ocean models. He has in fact proposed a rudimentary parameterization ([Holloway 1992](#)) but there has been little further progress in this direction. Nevertheless, model performance can be improved by the incorporation of this parameterization (e.g., [Eby and Holloway 1994](#); [Holloway et al. 1995](#); [Holloway and Sou 1996](#)).

On the other hand, there also exists the theory of turbulent gyre homogenization ([Rhines and Young 1982](#)). Under conditions of weak forcing and dissipation, Rhines and Young argue that it is possible to have a statistically steady state characterized by the existence of homogenized gyres, such that mean potential vorticity inside a gyre is constant; that is,

$$\frac{\partial \langle q \rangle}{\partial \langle \psi \rangle} = 0, \tag{5}$$

and the fluid is at rest outside the gyre, that is, $q = \beta y$, or $\langle \psi \rangle = 0$. The mechanism for homogenization is assumed to be a downgradient eddy flux of potential vorticity,

$$\langle \mathbf{u}'q' \rangle = -\kappa \nabla \langle q \rangle, \tag{6}$$

where κ is an eddy diffusivity (in general, a symmetric positive-definite tensor), similar to what is employed in conventional turbulence parameterizations. Such homogenized states have been observed both computationally and in observations (e.g., [Cessi et al. 1987](#); [O'Dwyer and Williams 1997](#)).

Thus, there is an apparent paradox: there are two different theoretical possibilities that are seemingly at odds with each other. On the one hand, equilibrium statistical mechanics suggests that there must be a linear relationship between mean potential vorticity and streamfunction throughout the flow, as in [(4)](#), whereas in the case of homogenized gyres there must be a strongly nonlinear relationship: $\langle q \rangle$ constant inside and $\langle \psi \rangle$ constant outside gyres. There have been a number of numerical studies to identify the existence of Fofonoff gyres in inviscid and weakly viscous free and forced turbulence arising from [Eq. (3)](#) (e.g., [Griffa and Salmon 1989](#); [Cummins 1992](#); [Wang and Vallis 1994](#)). In inviscid calculations, Fofonoff gyres appear to be generally observed. However, in viscous calculations both types of solutions are found, even in completely unforced turbulence ([Wang and Vallis 1994](#)). Similar results have been obtained in studies with a more complete ocean model ([Griffa et al. 1996](#)). These studies, therefore, do not resolve the paradox.

In this paper we reexamine the problem of unforced turbulence in a detailed numerical study to shed light on this problem, namely, under what conditions do flows of the Fofonoff-type or of the homogenized-gyre-type emerge. It turns out that the answer is largely a matter of timescale.

2. Preliminaries

It will be convenient to deal henceforth with nondimensional quantities, denoted temporarily by primes: $t' = tU/L$, $\mathbf{x}' = \mathbf{x}/L$, $\mathbf{u}' = \mathbf{u}/U$, $\psi' = \psi/LU$, $\zeta' = \zeta L/U$, $\mu' = \mu L^2$, where L is a length scale and U is a velocity scale. We shall choose L so that the domain area is L^2 and U is the initial rms velocity. Therefore the initial total energy is $E_0 = \frac{1}{2}U^2L^2$. The problem is characterized by a single nondimensional parameter, the Rossby number, $\mathrm{Ro} = U/\beta L^2$. Note that the time is normalized by a mean "eddy turnover time," $\tau_E = L/U$. Quasigeostrophic flow in the form of [(1)](#) or [(3)](#) possesses an infinite number of Lagrangian invariants, including, most importantly, the energy and potential enstrophy:

$$\frac{d}{dt}\left(\frac{1}{2}|\nabla \psi|^2\right) = \frac{d}{dt}\left(\frac{1}{2}q^2\right) = 0.$$

This implies the existence of global invariants of energy and potential enstrophy for a flow in a closed domain:

$$E = \frac{1}{2}\iint |\nabla \psi|^2 \, dA = E_0,$$

$$Q = \frac{1}{2}\iint q^2 \, dA = Q_0,$$

and equivalently

$$E' = \frac{1}{2} \iint |\nabla' \psi'|^2 \, dA' = E'_0,$$

$$Q' = \frac{1}{2} \iint q'^2 \, dA' = Q'_0,$$

for the nondimensional case, where Q_0, Q'_0 are the initial total potential enstrophies, and the integration is over the entire domain. This, together with the definition of E_0, implies that the amplitude of the initial nondimensional streamfunction must be such that $E' = E'_0 = \frac{1}{2}$. Dropping primes in what follows, we observe that Eqs. (1)–(4) retain their form in the nondimensional case, except that the potential vorticity becomes

$$q = \zeta + \frac{1}{\mathrm{Ro}} y.$$

Given the existence of the above invariants, statistical mechanics (Salmon et al. 1976) predicts that a turbulent flow will exist with a mean flow characterized by (4), which, without loss of generality, may be written as $\langle q \rangle = \mu \langle \psi \rangle$. In general, the energy and potential enstrophy of the mean flow, denoted by $\langle E \rangle$ and $\langle Q \rangle$, respectively, are lower than the total energy and potential enstrophy, the difference appearing as the energy or potential enstrophy of the fluctuations, denoted by E' and Q', respectively. Carnevale and Frederiksen (1987) discuss the problem in terms of presumed steady-state solutions, which satisfy the relationship $q = \mu \psi$. They show that when the wavenumber is confined between some maximum and minimum, $k_{max} > |k| > k_{min}$, then there exist two stable branches of solutions: a minimum potential enstrophy branch for $\mu > -k^2_{min}$, and a maximum potential enstrophy branch for $\mu < -k^2_{max}$. The minimum potential enstrophy branch corresponds to solutions postulated by Bretherton and Haidvogel (1976). The energy of the minimum potential enstrophy branch, $E^f(\mathrm{Ro}, \mu)$, where the superscript f stands for Fofonoff, is plotted in Fig. 1 ⦾ as a function of μ. Carnevale and Frederiksen (1987) then show that in the limit of infinite resolution, $k_{max} \rightarrow \infty$, the maximum potential enstrophy branch disappears and there are two possible cases of interest.

Case I: $E^f(\mathrm{Ro}, -k^2_{min}) \geq \frac{1}{2}$

In this case, $\langle E \rangle = E^f(\mathrm{Ro}, \mu) = \frac{1}{2}$. This means that the mean energy is equal to the total energy and therefore that the fluctuating energy E' is zero. This condition determines the value of μ. The mean potential enstrophy, $\langle Q \rangle = Q^f(\mathrm{Ro}, \mu) \leq Q$, and therefore $Q' \geq 0$. The fluctuating potential enstrophy Q' all appears at maximum wavenumber, that is, $k = \infty$. Therefore, the statistical steady state in this case is the result of an inverse cascade in energy in which all the energy ends up in the mean flow largely at large scales, and a direct cascade in potential enstrophy resulting in a mean flow at minimum potential enstrophy and the remaining potential enstrophy all in fluctuations at the highest wavenumbers. We expect that most if not all flows will belong to this category; this is certainly true of all the computational cases in this study.

Case II: $E^f(\mathrm{Ro}, -k^2_{min}) < \frac{1}{2}$

In this case, $\mu = -k^2_{min}$, and $E = \langle E \rangle + E'$, where $\langle E \rangle = E^f(\mathrm{Ro}, -k^2_{min})$. Thus the energy of the mean flow is less than the total energy, and the excess energy appears in the fluctuations at k_{min}. Similarly, the mean potential enstrophy is $\langle Q \rangle = Q^f(\mathrm{Ro}, -k^2_{min})$ but the fluctuating potential enstrophy is now divided between a part that appears at k_{min} and another part that appears at $k_{max} \rightarrow \infty$. However, this case is of academic interest to us since we do not observe it in the calculations.

The streamfunction of solutions on the minimum potential enstrophy branch is illustrated in Fig. 2 ⦾ for two values of μ. These were computed on a 64 cell × 64 cell grid, which we henceforth denote as the 64 × 64 grid, by discretizing and solving the Poisson equation:

$$\nabla^2 \psi - \mu \psi = -\frac{1}{\mathrm{Ro}} y,$$

with boundary condition $\psi = 0$. The contour plots are typical of what one expects to see in a solution with Fofonoff gyres. Note that negative values of μ are possible provided $\mu > -k^2_{min}$. The parameter k^2_{min} is associated with the smallest in magnitude of the eigenvalues of the discrete Laplacian (with boundary conditions equal to zero), and it depends on the resolution and on the maximum wavelengths in the two directions: $2L$ in the x direction, and L in the y direction. This gives $k^2_{min} \approx 49.3$ for the present case, in agreement with the computational results. The thickness of the inertial boundary layers is dependent on μ; the boundary layers become very thin for very large positive μ, with thickness proportional to $\mu^{-1/2}$. The potential enstrophy $Q^f(\text{Ro}, \mu)$ of these Fofonoff-gyre solutions, and the associated value of μ, such that $E^f(\text{Ro}, \mu) = \frac{1}{2}$ (obtained iteratively by varying μ until the correct energy is obtained), is given in Table 1 for the several values of the Rossby number and grid resolution used in this study. The potential enstrophy in the rest state, associated with the planetary vorticity βy, is given by $Q^p = \text{Ro}^{-2}/24$. We observe that the total potential enstrophy of these Fofonoff-gyre solutions is always lower than this value; this is consistent with these being minimum potential enstrophy solutions because the relative vorticity of the flow in the boundary layers is opposite in sign to the planetary vorticity, and therefore acts to reduce the magnitude of the local potential enstrophy. We also observe that the total potential enstrophy may be approximately collapsed through the functional relationship given by

$$\Upsilon = [Q^f(\text{Ro}, \mu) - Q^p]\text{Ro}^{3/2} \sim \text{const.} \quad (7)$$

This phenomenon can be understood by noting that the deviation from planetary potential enstrophy for large μ is primarily due to the boundary layers, where the magnitude of the relative vorticity is of order Ro^{-1} and the boundary layer thickness is of order $\text{Ro}^{1/2}$, so that the area integral of the deviation from planetary potential enstrophy is expected to scale as $\text{Ro}^{-3/2}$.

3. Inviscid calculations

A discrete model has been constructed that integrates (3) on a square domain of unit size at the resolutions and Rossby numbers listed in Table 1 , namely, at resolutions of 64×64, 128×128, 256×256, and Rossby numbers Ro = 1.59×10^{-3}, 3.18×10^{-3}, 7.95×10^{-3}, 1.59×10^{-3}, and 3.18×10^{-3}. This range of Rossby numbers is similar to that used in other studies (e.g., Cummins 1992; Wang and Vallis 1994). The spatial discretization is the energy and potential enstrophy conserving Arakawa scheme with boundary and corner operators as given by Salmon and Talley (1989). The time discretization is a third-order-accurate Runge–Kutta method with the time step automatically selected such that the relative vorticity error at second order is $\sim 10^{-3}$ percent. This ensures that energy and potential enstrophy is conserved to the fourth significant digit in all calculations. The time discretization is described in more detail in appendix A. Unless indicated otherwise, the data presented below have been time averaged over one eddy turnover time, that is, data shown at time t are averaged over the time from $t-1$ to t. This is typically equivalent to several thousand time steps in the inviscid runs. Longer averaging periods after the statistically steady state (SSS) is achieved merely serve to further reduce the scatter due to the fluctuating component.

The initial condition for the streamfunction is a harmonic function of the form

$$\psi = \psi_0 \sin(\pi k_x x) \sin(\pi k_y y), \quad (8)$$

where ψ_0 is a coefficient set such that total initial energy $E_0 = \frac{1}{2}$, and k_x, k_y specify the integer number of half-wavelengths (i.e., k_x, k_y are twice the initial wavenumbers) of the streamfunction in the respective coordinate directions, which serves to establish the magnitude of the initial potential enstrophy. Theoretically, as discussed above, at infinite resolution one expects that the statistically steady state should be independent of the initial condition, but this is not true at finite resolution. Figures 3–6 show the averaged energy, ⟨E⟩, and potential enstrophy, ⟨Q⟩, at Ro = 7.95×10^{-3} as a function of time, for several different initial mode numbers, $k_x = k_y = 4, 8, 16, 32,$ and 64, and for varying resolutions. In general, a reasonably good statistically steady state is reached by time $t = 30$.

In all cases, we find that the mean energy at SSS is lower than the total energy $E = \frac{1}{2}$, the difference appearing in the fluctuations. The mean energy is smaller at the higher initial wavenumbers and lower resolutions. However, the fluctuating energy uniformly decreases as the resolution is increased, indicating a convergence of the mean and the total energies, in agreement with the prediction of the theory. The averaged potential enstrophy typically drops from its initial value and in the SSS tends to approach the Fofonoff value Q^f as the resolution is increased. In most cases, the final potential enstrophy is lower than the planetary enstrophy Q^p and in these cases it is clear that a Fofonoff gyre flow has been established in the mean since this situation is expected from Fofonoff-gyre solutions, as discussed in the previous section. In some cases,

however, the SSS enstrophy is substantially higher than the planetary enstrophy, particularly at high initial wavenumber and low resolution. Nevertheless, as the resolution is increased the final enstrophy appears to uniformly approach the Fofonoff value Q^f. Figure 7 ⊙ shows scatterplots of ‹q› versus ‹ψ› for mode 32 × 32 at Ro = 7.95×10^{-3} at three different resolutions, corresponding to Fig. 6 ⊙ at time $t = 30$. This is a sufficiently high wavenumber mode that it begins to show a large departure from expected behavior at the low resolution case of 64 × 64, and it conveniently illustrates the convergence of the SSS as the resolution is increased. In all three cases the scatterplot indicates an approximately linear correlation between ‹q› and ‹ψ› in accord with the theory. At high resolution, the correlation is clearly linear with a positive slope of approximately 270, not very different from the corresponding value of about 215 from Table 1 ⊙, indicating that the mean flow is a Fofonoff gyre on the minimum potential enstrophy branch of possible solutions. At low resolution, the linear correlation is not as distinct but it does appear to give a correlation with a very large negative slope. This suggests that the mean flow in this case is on the maximum potential enstrophy branch. This impression is reinforced by the very chaotic nature of the contours of the averaged streamfunction at SSS, illustrated in Fig. 8 ⊙, as compared to the distinct mean Fofonoff state observed for the high-resolution case. Figure 9 ⊙ shows the averaged energy and potential enstrophy as a function of Rossby number for initial mode number 8 × 8 and resolution 128 × 128. In general, the behavior of the energy is insensitive to variations in the Rossby number, while the potential enstrophy is reasonably well collapsed by the relationship (7), except at the highest value of Rossby number, Ro = 0.0318. This departure from the scaling behavior at large values of Rossby number is likely to be removed as resolution is increased since the Rossby number sensitivity of the theoretical Fofonoff-gyre scaled potential enstrophy is much smaller, as indicated by the range of Y^f in the figure as well as in Table 1 ⊙.

In general, the numerical calculations in the inviscid case verify the theoretical predictions of the equilibrium statistical mechanical theory. This means that independent of initial conditions a mean flow is established in the form of Fofonoff gyres such that at infinite resolution the mean energy is equal to the total energy and the mean potential enstrophy is given by the minimum potential enstrophy consistent with the total energy. We observe that the adjustment to the final mean state appears to take place in two stages: (a) there is an initial rapid adjustment (see Fig. 4a ⊙, for example) in which turbulence is generated from smooth initial conditions by a process of barotropic instability causing a rapid drop in the time-averaged energy due to the generation of eddy energy while the total energy remains constant, (b) followed by a considerably slower adjustment to the statistically steady state, which is due primarily to the inertial cascade, in which eddy energy cascades to the large scales and appears to be recovered in the time-mean energy, and the enstrophy cascades to the small scales and therefore appears to be lost from the time-mean enstrophy. The timescale for this inertial-cascade adjustment is τ_0, approximately equal to 5–10τ_E, and it is roughly independent of Rossby number, initial conditions, or resolution, at least within the range of parameters considered in this study. This scaling is consistent with the discussion by Rhines (1979), who argues that adjustment takes place by a combination of linear (Rossby wave) and nonlinear processes. The linear process timescale is on the order of $\tau_\beta = 1/\beta L$, and the nonlinear timescale is $\tau_E = L/U$. The ratio of these timescales is τ_β / τ_E = Ro ≪ 1, and so the linear adjustment takes place very quickly as compared to the nonlinear adjustment. The overall adjustment is therefore controlled by τ_E, as observed in the present calculations.

4. Viscous calculations

When viscosity is present, we modify the nondimensional vorticity equation (3) as follows:

$$\partial_t \zeta + J(\psi, q) = \frac{1}{Re} \nabla^2 \zeta, \qquad (9)$$

where again $q = \zeta + (1/Ro)y$, and the Reynolds number Re = UL/ν is defined in terms of a kinematic viscosity coefficient ν, which may represent either a physical viscosity or the coefficient of an eddy viscosity parameterization. There is some arbitrariness in the choice of the viscous operator. In general, this term may be viewed as a subgrid parameterization. For numerical reasons, and in order to avoid the effects of viscous damping at large scales, a biharmonic viscosity term is frequently employed in eddy-resolving models. We will however confine ourselves to a Laplacian viscosity because it is the usual parameterization used in non-eddy-resolving models so that the results obtained here would be of direct relevance to models used in climate simulations, and because it limits to the physically correct representation of viscous effects so that the effects of boundary conditions are better understood. We are then faced with the difficult question of specifying the additional boundary condition that is needed because the viscous term in (9) contains spatial derivatives of higher order than the other terms in the equation. In the oceanic case, the viscous term amounts to a singular perturbation of Eq. (3), signifying that Re is typically so large that the solution must accomodate the additional condition in a very thin layer at the boundary. In numerical calculations it is generally impossible to resolve these layers, which nevertheless can change the entire character of the solution. Since it is not possible to resolve the viscous boundary layers, what is needed is an effective boundary condition that sets up the correct type of flow in the interior without having to resolve these layers. Bretherton and Haidvogel (1976) make it clear that the interior solutions of interest in the oceanic case are ones in which enstrophy may be strongly dissipated but where the energy is only weakly dissipated. In previous studies (e.g., Cummins 1992; Wang and

Vallis 1994), a variety of boundary conditions have been tried, such as no-slip, free-slip, and "super-slip." There are various difficulties with all of these boundary conditions. For example, it is generally not possible to ensure that both the energy and enstrophy are consistently dissipated. The main difficulty, however, is that the use of these boundary conditions requires that the viscous boundary layers be resolved, which implies prohibitively high resolution at small values of viscosity. This means that it is not possible to go over smoothly to the limit of zero viscosity because the need to resolve boundary layers requires that the viscosity cannot go below some minimum value, depending on the grid size used. In other words, the choice of viscosity is constrained by the grid size. We therefore chose to make use of a "numerical" solution to all the above problems by decoupling the discrete viscous operator at the boundaries from the one in the interior in such a way that both the energy and enstrophy are guaranteed to be dissipated, as they would be by the interior operator in the absence of boundaries, whatever the value of the viscosity or grid size. In a sense, therefore, the viscous smoothing becomes insensitive to the boundaries and hence permits the development of the type of solution envisioned by Bretherton and Haidvogel under all conditions. The above provides a motivation for choosing an alternative boundary treatment; the actual implementation is described in detail in appendix B.

The Reynolds number was varied over two orders of magnitude: $1/\text{Re} = 6 \times 10^{-6}$, 1.9×10^{-5}, 6×10^{-5}, 1.9×10^{-4}, and 6×10^{-4}, a sufficient range of variation to cover weak as well as strong effects of viscosity. The viscous cases were all initiated from the corresponding inviscid calculation at time $t = 30$. Although these calculations were done at two resolutions, 64×64 and 128×128, no significant differences between them were noted and therefore only the results at resolution 128×128 will be presented. Similarly, all the calculations were continuations of runs started from initial mode 8×8, because, as pointed out in the previous section, the effect of the initial mode on the mean flow is not large for this grid. Figure 10 shows the effect of varying the Reynolds number on the evolution of the averaged energy and potential enstrophy for the cases with Ro $= 7.95 \times 10^{-3}$. Figure 11 shows the corresponding results as the Rossby number is varied for the cases with $1/\text{Re} = 6 \times 10^{-5}$. It is indeed quite remarkable that the time evolution of all these viscous calculations can be scaled with the single timescale $\tau_v = \tau_\epsilon \text{RoRe} = \delta^2/\nu$, where δ is the Rhines scale, $\delta = (U/\beta)^{1/2}$, and by the use of the potential enstrophy scaling (7), as shown in Figs. 12 and 13. We have plotted the time axis in terms of a scaled time T, defined as $T = (t - 30)\tau_\epsilon/\tau_v$, so that the origin is located at the time when viscosity is switched on. Figure 12 shows the resulting collapse of the averaged energy and scaled potential enstrophy curves at Ro $= 7.95 \times 10^{-3}$ with varying Reynolds number, and Fig. 13 shows the corresponding quantities at $1/\text{Re} = 6 \times 10^{-5}$ with varying Rossby number. It is quite obvious from the effectiveness of the scaling for both the potential enstrophy and the energy that all the curves of both figures could be collapsed into a single set of figures, although this would lead to a very cluttered presentation.

Figures 12 and 13 suggest that the development of the flow field should be at a similar stage at a given value of T, independently of the values of the Rossby and Reynolds numbers. This is tested in Figs. 14, 15, and 16, for values of T equal to approximately 0.075, 0.25, and 0.45, respectively. The hypothesis appears to be approximately verified. It is apparent from these figures that the Fofonoff gyres become homogenized and then proceed to decay. This evolution of the Fofonoff gyres is traced in detail in Fig. 17 for the case with Ro $= 7.95 \times 10^{-3}$, $1/\text{Re} = 6 \times 10^{-5}$, and the 128×128 mesh. Starting from the inviscid SSS at $t = 30$, the Fofonoff gyres are effectively homogenized by $t \sim 40$ and then the homogenized gyres proceed to decay until very little flow remains by $t \sim 100$. The homogenized gyre solutions found in this study are essentially the same as those predicted or observed elsewhere: gyres of approximately uniform potential vorticity confined in bands of latitude next to the northern and southern boundaries, and separated by regions of no flow (Rhines and Young 1982; Fig. 14 in Wang and Vallis 1994).

There appear to be three qualitatively different regimes during the gyre evolution process:

1. A period of very rapid adjustment, illustrated in Fig. 18 on an expanded timescale in which we plot the total potential enstrophy, instead of the time-averaged potential enstrophy, since the timescale of the adjustment is shorter than the averaging period. This is the regime in which the enstrophy accumulated at very high wavenumbers by the inviscid cascade is dissipated by viscosity. The timescale for this process appears to be $\tau_1 \sim 0.005\tau_v$.

2. An intermediate period during which the gyres are homogenized. The timescale for this regime is approximately $\tau_2 \sim 0.04\tau_v$.

3. Finally, there follows a period during which the homogenized gyres decay away to zero flow. This occurs on a timescale $\tau_3 \sim 0.3\tau_v$.

It is instructive to consider the decay of a homogenized gyre in order to understand the emergence of the timescale τ_v and the prominent role it plays in the observed scaling. Let us consider a simplified gyre that is extended indefinitely in the zonal direction (i.e., ignoring the ends) so that the only velocity present is the u component, which depends on y only. As seen

quite clearly in Fig. 15 ⊙, for example, an idealized homogenized gyre consists of a narrow region of circulation of width Δ_y, containing uniform q, and located next to the upper or lower boundary. The remainder of the domain is at rest. Reverting to dimensional variables, it is easy to show that the width of the gyre is

$$\Delta_y = \left(\frac{3U_0}{\beta}\right)^{1/2}, \qquad (10)$$

where U_0 is the magnitude of the velocity at the boundary [an analogous expression in terms of rms velocity is obtained by Cummins (1992)]. In appendix B, Eq. (B7a) shows that we must have

$$\frac{\partial E}{\partial t} = \frac{\partial}{\partial t} \int_{L/2-\Delta_y}^{L/2} \frac{u^2}{2}\, dy = -\nu \int_{L/2-\Delta_y}^{L/2} \left(\frac{\partial u}{\partial y}\right)^2 dy, \quad (11)$$

where here E is the total energy of a single gyre per unit length in the zonal direction. Thus, approximating the gyre as being composed of two counterflowing jets of strength U_0 and width $\Delta_y/2$, we have approximately

$$\frac{\partial E}{\partial t} \approx -\nu \left(\frac{4U_0}{\Delta_y}\right)^2 \Delta_y, \qquad E \approx \frac{1}{2}U_0^2 \Delta_y. \qquad (12)$$

Combining (10) and (12), we obtain

$$\frac{\partial E}{\partial t} \approx -\frac{32}{3}\frac{\nu\beta}{U_0}E \approx -\frac{E}{0.1\tau_\nu}, \qquad (13)$$

where we ignore the distinction between U_0 and U in this rough estimate. This suggests that the timescale for the decay is approximately $0.1\tau_\nu$, of the same order of magnitude as that found in the calculations. The timescale τ_ν is therefore closely associated with the emergence of the natural length scale of the problem, that is, the width of the homogenized gyre, which is on the order of the Rhines scale, $\delta = (U_0/\beta)^{1/2}$.

5. Emergence of Fofonoff/homogenized gyres from initial conditions

In the previous section we have shown that if viscosity is turned on after Fofonoff gyres are established, the gyres become homogenized and decay on a timescale that varies inversely with the viscosity. Now we will investigate whether Fofonoff gyres emerge if viscosity is present from the beginning. Figure 19 ⊙ shows the results for the time-averaged energy and potential enstrophy for several runs with Ro $= 7.95 \times 10^{-3}$ at resolution 128×128, started from initial mode 8×8, with zero viscosity as well as with several finite values of viscosity corresponding to $1/\mathrm{Re} = 1.9 \times 10^{-6}$, 6×10^{-6}, 1.9×10^{-5}, and 6×10^{-5}. In Fig. 20 ⊙ we show the corresponding scatterplots of $\langle q \rangle$ versus $\langle \psi \rangle$ at $t = 30$. When plotted versus the nondimensional time t in Fig. 19 ⊙, the inviscid energy plot forms an approximate envelope for the viscous calculations, indicating that the inertial timescale τ_E is appropriate for the initial transient. As before, SSS is achieved in the inviscid case at approximately $t = 30$, yielding the Fofonoff mean state observed in Fig. 20a ⊙. For the lowest value of viscosity, $1/\mathrm{Re} = 1.9 \times 10^{-6}$, a Fofonoff solution nearly manages to emerge by this time, as seen in Fig. 20b ⊙, and it then proceeds to homogenize and decay. At larger values of viscosity, a Fofonoff solution never appears, and instead a fully homogenized gyre emerges, as seen in Fig. 20d ⊙. If the viscosity is sufficiently high, a largely decayed homogenized gyre emerges, as in Fig. 20e ⊙.

It is interesting to observe that even a very small value of viscosity, as in Fig. 20b ⊙, is effective in removing the fluctuations as they cascade to small scales. This leaves a mean state that is even closer to the theoretical prediction than is the inviscid mean state, as is clearly seen in Fig. 19b ⊙. Namely, we see that the potential enstrophy approaches the theoretical value Q^f much closer in the viscous runs than in the inviscid run, in which a substantial amount of enstrophy is tied up in the fluctuations.

It appears that the emergence of Fofonoff versus homogenized gyres is a result of a competition between the statistical tendency to form Fofonoff gyres and the tendency of viscosity to homogenize these gyres. The competition depends on the

relative magnitude of two timescales: observe that $\tau_2 = 5.6\tau_0$ in Fig. 20b **O⁻**, when Fofonoff gyres emerge, and $\tau_2 = 0.6\tau_0$ in Fig. 20d **O⁻**, when homogenized gyres emerge from initial conditions. Therefore, Fofonoff gyres emerge if the timescale for homogenization τ_2 is longer than the inertial timescale τ_0, and homogenized gyres emerge if the converse is true. This is not inconsistent with previous work (Cummins 1992; Wang and Vallis 1994) in which both Fofonoff gyres and homogenized gyres were observed to emerge from arbitrary initial conditions in viscous calculations.

6. Discussion and conclusions

In this relatively simple model we have found that it is possible for both Fofonoff gyres and homogenized gyres to exist in a turbulent quasigeostrophic flow depending on the magnitude of the horizontal viscosity. In the absence of viscosity, the mean flow is organized into Fofonoff gyres on a timescale of $\tau_0 = 5$–$10\tau_E$ and such a flow persists indefinitely. In the presence of viscosity, existing Fofonoff gyres become homogenized on a timescale of $\tau_2 = 0.04\tau_\nu$, and then decay on a timescale of approximately $\tau_3 = 0.3\tau_\nu$, for any value of the viscosity. In general, in the presence of viscosity, we observed a competition between the tendency of the mean flow to form Fofonoff gyres and the tendency toward homogenization, with homogenization always winning out given a sufficiently long time. It is merely a question of timescale: (a) if $\tau_0 < \tau_2$ then Fofonoff gyres will be formed and will persist for a significant time, to be eventually replaced by homogenized gyres;(b) if $\tau_0 > \tau_2$ then homogenized gyres will be formed directly, overwhelming the statistical tendency to form Fofonoff gyres.

The question naturally arises as to which of these regimes is more relevant in the ocean. Assuming representative values: $U = 0.1$ m s^{-1}, $L = 10^3$ km, $\beta = 10^{-11}$ m^{-1} s^{-1}, and a molecular viscosity $\nu = 10^{-6}$ m^2 s^{-1}, we see that $\tau_E = 10^7$ s and $\tau_\nu = 10^{16}$ s. Therefore, Fofonoff gyres of this size would tend to form on a timescale of 1–3 yr, and the homogenization timescale is on the order of millions of years. Obviously, if molecular viscosity is the only effective horizontal dissipative mechanism, then the statistical tendency to form Fofonoff gyres will greatly dominate. However, there is strong evidence to the contrary from observations of homogenization on large scales (e.g., McDowell et al. 1982; Keffer 1985). This suggests that there must exist some effective horizontal viscosity that is much larger than molecular viscosity in order to shorten the homogenization timescale so that it becomes competitive or dominates the statistical tendency to organize mean flows at these large scales. This does not preclude the possibility that the statistical tendency will play an important role in the ocean at smaller scales. Observe that the timescale for the formation of the statistically generated Fofonoff gyres, τ_0, is directly proportional to the gyre scale, L, while the homogenization timescale, τ_2, does not directly depend on this length scale. Thus, there is a possibility, which we have not studied, that topographic forcing at much shorter length scales would involve inertial equilibration times shorter than the homogenization time. While it is difficult to directly observe such "Neptune" flows, there is indirect evidence that they exist because including their effects appears to improve model skill when applied to current meter data, for example, Holloway and Sou (1996).

One can speculate on the possible mechanisms for an effective viscosity responsible for large-scale homogenization. One possibility involves the three-dimensional energy cascade, which, if it exists, must do so time and length scales that break both the quasigeostrophic and hydrostatic approximations. Quasigeostrophy will fail for length scales $l < U/f$, where f is the Coriolis parameter, or for timescales $\tau < 1/f$. Assuming unforced turbulence, in which case $\tau \sim l/U$, allows these criteria to become equivalent. The hydrostatic assumption will be violated for $l \ll H$, where H is the ocean depth. Taking $f = 10^{-4}$ s^{-1}, the length scale for the breakdown of quasigeostrophy is approximately $l < 1$ km, whereas l need only be less than about 4 km for the hydrostatic approximation to fail. A rough estimate for the effective eddy viscosity is $\nu \sim Ul$ (when the dissipation rate associated with this viscosity is roughly equivalent to the inertial cascade of energy to scales in the dissipation range). Taking $l \sim 100$ m, this gives $\nu \sim 10$ m^2 s^{-1}, implying a homogenization timescale τ_2 of 1 year or so, which is sufficient to account for the observed homogenization on large scales. Of course, it is possible that other dissipative mechanisms, such as internal wave breaking or processes occurring at boundaries or near the surface, might be responsible.

The existence of these two regimes dependent on the relative magnitude of τ_0 and τ_2 has implications for turbulence parameterizations involving downgradient transport of potential vorticity, such as expressed in (6). It is easy to show that inviscid flow, which characterizes regime (a), is inconsistent with parameterization (6). Equation (1), and together with the fact that the velocity field is divergence-free, may be ensemble or time-averaged to give

$$\partial_t \langle q \rangle + \nabla \cdot (\langle \mathbf{u} \rangle \langle q \rangle + \langle \mathbf{u}'q' \rangle) = 0.$$

In the statistically steady state, $\partial_t \langle q \rangle = 0$, and because of (4), we must have $\nabla \cdot \langle \mathbf{u} \rangle \langle q \rangle = 0$, implying $\nabla \cdot \langle \mathbf{u}'q' \rangle = 0$. Therefore, downgradient potential vorticity mixing, that is, (6), requires that

$$\nabla \cdot \kappa\mu\nabla\langle\psi\rangle = 0.$$

Because κ is positive and μ is a constant, this, together with the boundary condition $\langle\psi\rangle = 0$, implies that $\langle\psi\rangle = 0$ everywhere. Another argument, based on the steady-state balance in the eddy-enstrophy variance equation, as in Rhines and Holland (1979), or in the stochastic theory of Dukowicz and Smith (1997), leads to the same conclusion. Thus, parameterization (6) implies zero mean flow in the inviscid case, in direct contradiction to the manifest existence of the mean flow in the form of Fofonoff gyres. This is consistent with the point made by Rhines and Holland (1979) that "the eddytransport of potential vorticity must have a component down the mean gradient, provided that friction acts to dissipate the potential enstrophy." The converse is presumably also true, that is, dissipation of potential vorticity by viscosity (or some other form of friction) is a precondition for the downgradient transport of potential vorticity. The evidence from this study suggests that a finite viscosity is essential for homogenization to occur (namely, homogenization is absent in inviscid flows of the type considered here). Rhines and Young (1982) show that downgradient transport of potential vorticity, (6), is sufficient for homogenization. This suggests, although it does not prove, that viscous dissipation is necessary for the downgradient eddy transport of potential vorticity and therefore that a parameterization of the type given by (6) may be suitable for flows in regime (b) but certainly not for regime (a).

Considerations such as these are relevant for eddy-viscosity parameterizations. For example, a typical value for a 1° lat × 1.2° long medium-resolution noneddy resolving model is $\nu = 10^4$ m^2 s^{-1} (e.g., Cox 1985; Böning et al. 1996). The homogenization timescale is then only about 10 h, putting the model strongly in regime (b) and implying strong decay of all homogenized gyres in the absence of forcing. Such a large viscosity may well be excessive. Eddy-resolving models, on the other hand, do have the potential to be in regime (a) at least for the large scales because of their reduced effective viscosity. This suggests a need for a similar study to evaluate the rate of homogenization with biharmonic mixing.

Acknowledgments

REFERENCES

Böning, C. W., F. O. Bryan, W. R. Holland, and R. Doscher, 1996: Deep-water formation and meridional overturning in a high-resolution model of the North Atlantic. *J. Phys. Oceanogr.,* **26,** 1142–1164.. Find this article online

Bretherton, F. P., and D. B. Haidvogel, 1976: Two-dimensional turbulence above topography. *J. Fluid Mech.,* **78,** 129–154..

Carnevale, G. F., and J. S. Frederiksen, 1987: Nonlinear stability and statistical mechanics of flow over topography. *J. Fluid Mech.,* **175,** 157–181..

Cessi, P., R. Ierley, and W. R. Young, 1987: A model of the inertial recirculation driven by potential vorticity anomalies. *J. Phys. Oceanogr.,* **17,** 1640–1652.. Find this article online

Cox, M. D., 1985: An eddy resolving numerical model of the ventilated thermocline. *J. Phys. Oceanogr.,* **15,** 1312–1324.. Find this article online

Cummins, P. F., 1992: Inertial gyres in decaying and forced geostrophic turbulence. *J. Mar. Res.,* **50,** 545–566..

Dukowicz, J. K., and R. D. Smith, 1997: Stochastic theory of compressible turbulent fluid transport. *Phys. Fluids,* **9,** 3523–3529..

Eby, M., and G. Holloway, 1994: Sensitivity of a large-scale ocean model to a parameterization of topographic stress. *J. Phys. Oceanogr.,* **24,** 2577–2588.. Find this article online

Fofonoff, N. P., 1954: Steady flow in a frictionless homogeneous ocean. *J. Mar. Res.,* **13,** 254–262..

Griffa, A., and R. Salmon, 1989: Wind-driven ocean circulation and equilibrium statistical mechanics. *J. Mar. Res.,* **47,** 457–492..

—— ,E. P. Chassignet, V. Coles, and D. B. Olson, 1996: Inertial gyre solutions from a primitive equation ocean model. *J. Mar. Res.,* **54,** 653–677..

Holloway, G., 1986: Eddies, waves, circulation, and mixing: Statistical geofluid mechanics. *Annu. Rev. Fluid Mech.,* **18,** 91–147..

—— ,1992: Representing topographic stress for large-scale ocean models. *J. Phys. Oceanogr.,* **22,** 1033–1046.. Find this article online

— , and T. Sou, 1996: Measuring the skill of a topographic stress parameterization in a large scale ocean model. *J. Phys. Oceanogr.,* **26,** 1088–1092.. Find this article online

— , — , and M. Eby, 1995: Dynamics of circulation of the Japan Sea. *J. Mar. Res.,* **53,** 539–569..

Keffer, T., 1985: The ventilation of the world's oceans: Maps of the potential vorticity field. *J. Phys. Oceanogr.,* **15,** 509–523.. Find this article online

Le Bail, R. C., 1972: Use of fast Fourier transforms for solving partial differential equations in physics. *J. Comput. Phys.,* **9,** 440–465..

McDowell, S., P. Rhines, and T. Keffer, 1982: North Atlantic potential vorticity and its relation to the general circulation. *J. Phys. Oceanogr.,* **12,** 1417–1436.. Find this article online

O'Dwyer, J., and R. G. Williams, 1997: The climatological distribution of potential vorticity over the abyssal ocean. *J. Phys. Oceanogr.,* **27,** 2488–2506.. Find this article online

Onsager, L., 1949: Statistical hydrodynamics. *Nuovo Cimento,* **6** (Suppl.), 279–287..

Rhines, P. B., 1979: Geostrophic turbulence. *Annu. Rev. Fluid Mech.,* **11,** 401–441..

— , and W. R. Holland, 1979: A theoretical discussion of eddy-induced circulation. *Dyn. Atmos. Oceans,* **3,** 289–325..

— , and W. R. Young, 1982: Homogenization of potential vorticity in planetary gyres. *J. Fluid Mech.,* **122,** 347–367..

Salmon, R., and L. D. Talley, 1989: Generalizations of Arakawa's Jacobian. *J. Comput. Phys.,* **83,** 247–259..

— , G. Holloway, and M. C. Hendershott, 1976: The equilibrium statistical mechanics of simple quasi-geostrophic models. *J. Fluid Mech.,* **75,** 691–703..

Wang, J., and G. K. Vallis, 1994: Emergence of Fofonoff states in inviscid and viscous ocean circulation models. *J. Mar. Res.,* **52,** 83–127..

APPENDIX A

7. Time-Discretization and Time-Step Control

The preservation of total energy and potential enstrophy in inviscid calculations is dependent on the accuracy of the time discretization, which we would like to control closely by choosing the time step appropriately. The spatially discretized version of Eq. (9) may be written in a general form as the following coupled system of ODEs:

$$\frac{\partial \zeta_{ij}}{\partial t} = F_{ij}[\psi(\zeta), \zeta], \qquad (A1)$$

where ζ_{ij} is the relative vorticity at node ij in the mesh, F_{ij} represents the total tendency as a combination of the advection and viscous terms, and ψ, ζ represent vectors of values of the streamfunction and relative vorticity, respectively, on the mesh. Note that ψ is implicitly a function of ζ through the discrete version of Eq. (2), together with the boundary condition on the streamfunction, $\psi = 0$. The resulting discrete Poisson equation [i.e., (B3)] may be solved using any one of the available rapid elliptic solvers; we use a combination of FFT in one spatial direction and a tridiagonal solver in the other direction (Le Bail 1972). To integrate the system (A1) we make use of the following third-order Runge–Kutta method:

$$\mathbf{K} = \mathbf{F}[\psi(\zeta^n), \zeta^n], \qquad \zeta^* = \zeta^n + \frac{1}{2}\Delta t^n \mathbf{K},$$

$$\mathbf{L} = \mathbf{F}[\psi(\zeta^*), \zeta^*], \qquad \zeta^{**} = \zeta^n - \Delta t^n \mathbf{K} + 2\Delta t^n \mathbf{L},$$

$$\mathbf{M} = \mathbf{F}[\psi(\zeta^{**}), \zeta^{**}],$$

$$\zeta^{n+1} = \zeta^n + \frac{1}{6}\Delta t^n (\mathbf{K} + 4\mathbf{L} + \mathbf{M}) + O(\Delta t^4), \qquad (A2)$$

where we have dispensed with the subscripts, and where the superscripts n and $n + 1$ refer to the time level. We also note that the second-order Runge–Kutta calculation:

$$\zeta^{***} = \zeta^n + \Delta t^n \mathbf{L} = \zeta^{n+1} + O(\Delta t^3), \quad (A3)$$

where $\mathbf{L}$ is the same as in (A2), provides a second-order accurate estimate (ζ^{***}) for ζ^{n+1} without the expense of additional functional evaluations, and therefore gives a simple and inexpensive estimate of the time-discretization error. We therefore estimate a global measure of the error as follows:

$$\text{error} = \frac{\max(|\zeta^{n+1} - \zeta^{***}|)}{\max(|\zeta^{n+1}|)}, \quad (A4)$$

where the maximum is taken over all values on the mesh. We choose an error criterion ε and the time step for the following integration of the equations is then given as follows:

$$\Delta t^{n+1} = \begin{cases} 0.8\Delta t^n & \text{if error} > 2\varepsilon, \\ 1.2\Delta t^n, & \text{if error} < 0.5\varepsilon, \\ \Delta t^n, & \text{otherwise.} \end{cases} \quad (A5)$$

Choosing an arbitrary initial Δt, we find that the time step quickly stabilizes, and the code continues running with only infrequent changes in the time step. We found that the choice $\varepsilon = 10^{-5}$ was sufficient to conserve energy and potential enstrophy to within four significant digits.

APPENDIX B

8. Effective Boundary Conditions for the Viscous Operator

It is physically desirable to have boundary conditions for (9) that avoid the singularity at $\text{Re} \rightarrow \infty$ when wall boundary layers are not resolved, and which also dissipate both energy and enstrophy under all conditions. We develop such boundary conditions in this appendix. It is much more convenient to develop the following argument in matrix notation. The spatially discretized form of (9) comes from an area integral and is given by

$$\partial_t(\mathbf{H}\zeta) + \mathbf{A}\zeta = \mathbf{D}\zeta, \quad (B1)$$

where $\mathbf{A}$ (for Arakawa) is the matrix representing the energy and potential enstrophy conserving advection operator, $\mathbf{D}$ is the matrix representing the discrete viscous or dissipation operator, and $\mathbf{H}$ is a diagonal matrix that represents the cell area, which will differ at the boundary and corners from the area in the interior of the domain. Note that this equation already incorporates the boundary conditions in the structure of the matrices. For simplicity, the matrices $\mathbf{A}$, $\mathbf{D}$, and other matrices introduced later absorb the area of the grid boxes. The relative vorticity ζ is a vector such that $\zeta = [\zeta_i, \zeta_b]^T$, where ζ_i represents a vector containing the values of ζ on the interior nodes of the mesh, and ζ_b represents a vector containing the values of ζ on the boundary nodes. The superscript T indicates a transpose. Similarly, the streamfunction is represented as a vector by $\psi = [\psi_i, 0]^T$, where the second component is zero because of the boundary condition, $\psi_b = 0$. Because of the properties of the Arakawa operator, we observe that

$$\zeta^T \mathbf{A}\zeta = \psi^T \mathbf{A}\zeta = 0. \quad (B2)$$

The definition of the relative vorticity (2) may be expressed as follows:

$$\mathbf{H}_i \zeta_i = -\mathbf{G}^T \mathbf{G} \psi_i, \quad (B3)$$

where $\mathbf{G}$ is a matrix representation of the discrete gradient, including the boundary conditions, and $\mathbf{H}_i$ is the diagonal matrix representing the area of the interior cells. It is always possible to write (2) in this way because we know that our

discretization of the Laplacian is symmetric and negative definite. The total energy and enstrophy are given by

$$E = -\frac{1}{2}\boldsymbol{\psi}^{\mathrm{T}}\mathbf{H}\boldsymbol{\zeta} = -\frac{1}{2}\psi_i^{\mathrm{T}}\mathbf{H}_i\zeta_i = \psi_i^{\mathrm{T}}\mathbf{G}^{\mathrm{T}}\mathbf{G}\psi_i$$

$$= (\mathbf{G}\psi_i)^{\mathrm{T}}\mathbf{G}\psi_i > 0, \tag{B4a}$$

$$Q = \frac{1}{2}\boldsymbol{\zeta}^{\mathrm{T}}\mathbf{H}\boldsymbol{\zeta} > 0. \tag{B4b}$$

The matrix $\mathbf{D}$ may be expressed quite generally as

$$\mathbf{D} = \frac{1}{\mathrm{Re}}\begin{bmatrix} -\mathbf{G}^{\mathrm{T}}\mathbf{G} & \mathbf{C} \\ \mathbf{C}^{\mathrm{T}} & -\mathbf{B}^{\mathrm{T}}\mathbf{B} \end{bmatrix}, \tag{B5}$$

where $-\mathbf{B}^{\mathrm{T}}\mathbf{B}$ is a dissipative matrix involving just the boundary points, and $\mathbf{C}$ is a matrix coupling the interior to the boundary points.

Observing that

$$\boldsymbol{\psi}^{\mathrm{T}\partial_t}\mathbf{H}\boldsymbol{\zeta} = -\psi_i^{\mathrm{T}}\mathbf{G}^{\mathrm{T}}\partial_t\mathbf{G}\psi_i = -\partial_t(\mathrm{\ddot{A}})(\mathbf{G}\psi_i)^{\mathrm{T}}\mathbf{G}\psi_i$$

$$= -\partial_t E, \tag{B6a}$$

and

$$\boldsymbol{\zeta}^{\mathrm{T}}\partial_t\mathbf{H}\boldsymbol{\zeta} = \partial_t(\tfrac{1}{2})\boldsymbol{\zeta}^{\mathrm{T}}\mathbf{H}\boldsymbol{\zeta} = \partial_t Q, \tag{B6b}$$

we multiply [(B1)](#) by $\boldsymbol{\psi}^{\mathrm{T}}$ and $\boldsymbol{\zeta}^{\mathrm{T}}$, respectively, and using [(B2)](#), we obtain

$$\partial_t E = -\boldsymbol{\psi}^{\mathrm{T}}\mathbf{D}\boldsymbol{\zeta} = -\frac{1}{\mathrm{Re}}(\mathbf{G}^{\mathrm{T}}\mathbf{G}\psi_i)^{\mathrm{T}}\mathbf{G}^{\mathrm{T}}\mathbf{G}\psi_i - \frac{1}{\mathrm{Re}}\psi_i^{\mathrm{T}}\mathbf{C}\zeta_b$$

$$= -\frac{1}{\mathrm{Re}}\zeta_i^{\mathrm{T}}\mathbf{H}_i^{\mathrm{T}}\mathbf{H}_i\zeta_i - \frac{1}{\mathrm{Re}}\psi_i^{\mathrm{T}}\mathbf{C}\zeta_b, \tag{B7a}$$

and

$$\partial_t Q = \boldsymbol{\zeta}^{\mathrm{T}}\mathbf{D}\boldsymbol{\zeta}$$

$$= -\frac{1}{\mathrm{Re}}(\zeta_i^{\mathrm{T}}\mathbf{G}^{\mathrm{T}}\mathbf{G}\zeta_i + \zeta_b^{\mathrm{T}}\mathbf{B}^{\mathrm{T}}\mathbf{B}\zeta_b) + \frac{2}{\mathrm{Re}}\zeta_i^{\mathrm{T}}\mathbf{C}\zeta_b. \tag{B7b}$$

Note that the leading terms on the rhs are negative-definite and therefore are always dissipative, whereas the remaining terms are of indefinite sign and could cause an unphysical increase in the energy or enstrophy. The simplest "boundary condition" that would enforce dissipation of both energy and enstrophy is the choice $\mathbf{C} = 0$. This is in fact what we have implemented; a choice that is equivalent to a boundary condition because it affects the system of equations only at the boundary.

The stencils for the operators are as follows, where ϕ is any node variable such as ψ or ζ: (a) Interior (i, j):

$$+ \frac{\Delta x}{\Delta y}(\alpha_{i,j-1}\phi_{i,j-1} - 2\phi_{i,j} + \alpha_{i,j+1}\phi_{i,j+1}),$$

(B8a)

where

$$\alpha_{i,j} = \begin{cases} 1 & \text{if } i \text{ and } j \text{ are in the interior} \\ 0 & \text{if } i \text{ or } j \text{ are on the boundary;} \end{cases}$$

(b) Boundary (i, j):

$$(-\mathbf{B}^{\mathrm{T}}\mathbf{B}\phi)_{i,j}$$

$$= \frac{\Delta y}{2\Delta x}[\beta_{i-1,j}(\phi_{i-1,j} - \phi_{i,j}) + \beta_{i+1,j}(\phi_{i+1,j} - \phi_{i,j})]$$

$$+ \frac{\Delta x}{2\Delta y}[\beta_{i,j-1}(\phi_{i,j-1} - \phi_{i,j}) + \beta_{i,j+1}(\phi_{i,j+1} - \phi_{i,j})],$$

(B8b)

where

$$\beta_{i,j} = \begin{cases} 1 & \text{if } i \text{ and } j \text{ are on the boundary} \\ 0 & \text{if } i \text{ or } j \text{ are off the boundary.} \end{cases}$$

The factor of ½ comes about because this operator is derived from cells associated with the gradient of ϕ; these cells straddle the boundary and so they contribute only one-half of their area.

Summing the stencils (B8) operating on the relative vorticity ζ over the entire mesh, we observe that the viscous term does not sum to zero and therefore that the present boundary condition does not conserve total vorticity. However, this is not to be expected except for the special case of the super-slip boundary condition, $\partial\zeta/\partial n = 0$.

Tables

Table 1. Total potential enstrophy of Fofonoff-gyre flow, specified by $E = \frac{1}{2}$ and $\nabla^2\psi + 1/\text{Ro } y = \mu\,\psi$, with boundary condition $\psi = 0$.

Mesh	μ	Q^I	Θ^I
(a) Ro = 0.00159; Q^p = 1.65 × 10⁴			
64 × 64	2233.0	1.260 × 10⁴	−0.246
128 × 128	2319.0	1.273 × 10⁴	−0.238
256 × 256	2343.0	1.276 × 10⁴	−0.236
(b) Ro = 0.00318; Q^p = 4.12 × 10³			
64 × 64	854.6	2.667 × 10³	0.261
128 × 128	869.6	2.686 × 10³	−0.257
256 × 256	873.5	2.690 × 10³	−0.256
(c) Ro = 0.00795; Q^p = 6.59 × 10²			
64 × 64	213.2	2.665 × 10²	−0.278
128 × 128	214.6	2.678 × 10²	−0.277
256 × 256	214.9	2.682 × 10²	−0.277
(d) Ro = 0.0159; Q^p = 1.65 × 10²			
64 × 64	58.47	2.655 × 10¹	−0.277
128 × 128	58.70	2.668 × 10¹	−0.277
256 × 256	58.76	2.671 × 10¹	−0.277
(e) Ro = 0.0318; Q^p = 4.12 × 10¹			
64 × 64	−1.265	1.464 × 10⁻²	−0.234
128 × 128	−1.224	1.369 × 10⁻²	−0.234
256 × 256	−1.214	1.345 × 10⁻²	−0.234

Click on thumbnail for full-sized image.

Figures
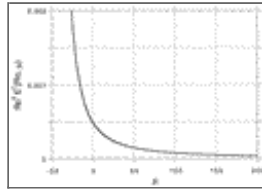
Fig. 1. The total energy on the minimum enstrophy branch of solutions, $\mu > -k^2_{min}$, as a function of μ, from a numerical solution on a 64×64 grid.
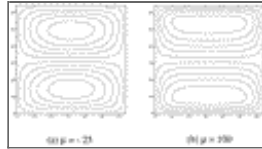
Fig. 2. Streamfunction contours at two values of μ on the minimum enstrophy branch of solutions, computed on a 64×64 grid, illustrating typical Fofonoff-gyre solutions. The inertial boundary layers are very thick at $\mu = -25$ and become progressively thinner for large positive μ, characteristic of the classical Fofonoff solution.
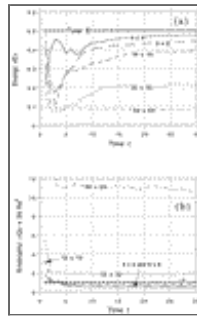
Fig. 3. Inviscid, time-averaged, domain-integrated energy (a) and potential enstrophy (b) for the 128×128 grid resolution at Ro = 0.007 95 at different initial mode numbers, $k_x \times k_y$, such that $k_x = k_y$, plotted as a function of nondimensional time t.
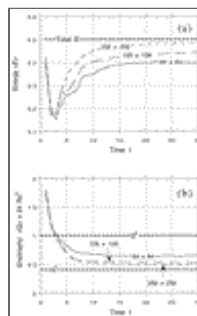
Fig. 4. Inviscid, time-averaged, domain-integrated energy (a) and potential enstrophy (b) for the 8×8 initial mode at Ro = 0.007 95 at different grid resolutions, plotted as a function of nondimensional time t.

Fig. 5. Inviscid, time-averaged, domain-integrated energy (a) and potential enstrophy (b) for the 16×16 initial mode at Ro = 0.007 95 at different grid resolutions, plotted as a function of nondimensional time t.
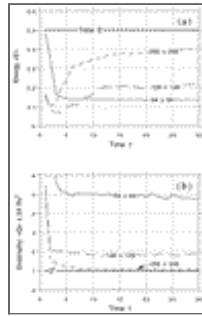
Fig. 6. Inviscid, time-averaged, domain-integrated energy (a) and potential enstrophy (b) for the 32×32 initial mode at Ro = 0.007 95 at different grid resolutions, plotted as a function of nondimensional time t.
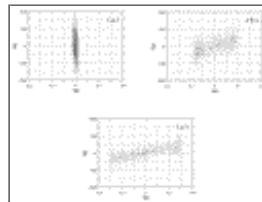
Fig. 7. Scatterplots of time-averaged, inviscid «q» versus «ψ», for initial mode 32×32, Ro = 7.95×10^{-3}, nondimensional time t = 30, for grid resolutions (a) 64×64, (b) 128×128, and (c) 256×256.
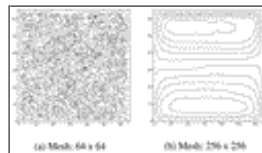
Fig. 8. Time-averaged inviscid streamfunction contours for two of the cases shown in Fig. 7 , (a) grid resolution 64×64 and (b) 256×256.
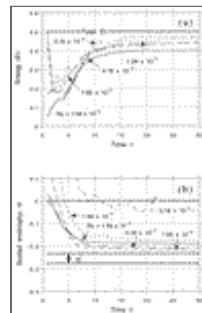
Fig. 9. Inviscid, time-averaged, domain-integrated energy (a) and scaled potential enstrophy (b) for the 8×8 initial mode and grid resolution 128×128, for different Rossby numbers, plotted as a function of nondimensional time t. The potential enstrophy is scaled according to Eq. (7).
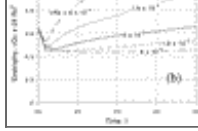
Fig. 10. Viscous, time-averaged, domain-integrated energy (a) and potential enstrophy (b) at Ro = 7.95 × 10^{-3} and grid resolution 128 × 128, for different Reynolds numbers, plotted as a function of nondimensional time t, having started from the corresponding inviscid case at $t = 30$.
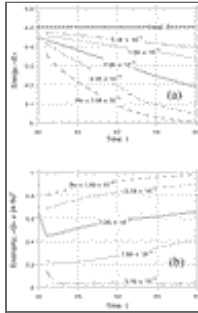
Fig. 11. Viscous, time-averaged, domain-integrated energy (a) and potential enstrophy (b) at 1/Re = 6 × 10^{-5} and grid resolution 128 × 128, for different Rossby numbers, plotted as a function of nondimensional time t, having started from the corresponding inviscid case at $t = 30$.
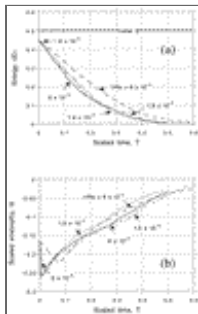
Fig. 12. Same as Fig. 10 except that the potential enstrophy is scaled according to Eq. (7), and the time is scaled such that $T = (t - 30)\tau_E/\tau_v$.
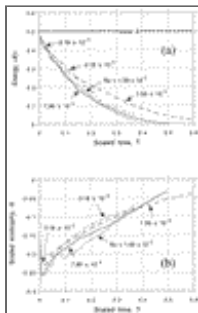
Fig. 13. Same as Fig. 11 except that the potential enstrophy is scaled according to Eq. (7), and the time is scaled such that $T = (t - 30)\tau_E/\tau_v$.
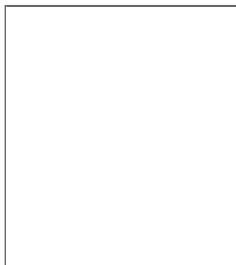
Fig. 14. The viscous development of Fofonoff gyres at $T \sim 0.075$. Scatterplots of time-averaged ‹q› vs ‹ψ› from 128×128 grid calculations. (a) $T = 0.075$, $t = 31$, Ro $= 0.007\ 95$, $1/\mathrm{Re} = 6 \times 10^{-4}$; (b) $T = 0.075$, $t = 50$, Ro $= 0.0159$, $1/\mathrm{Re} = 6 \times 10^{-5}$; (c) $T = 0.072$, $t = 33$, Ro $= 7.95 \times 10^{-3}$, $1/\mathrm{Re} = 1.9 \times 10^{-4}$; (d) $T = 0.075$, $t = 34$, Ro $= 0.003\ 18$, $1/\mathrm{Re} = 6 \times 10^{-5}$; (e) $T = 0.075$, $t = 32$, Ro $= 0.001\ 59$, $1/\mathrm{Re} = 6 \times 10^{-5}$.
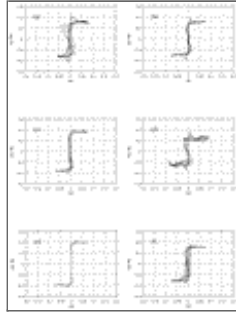
Fig. 15. The viscous development of Fofonoff gyres at $T \sim 0.25$. Scatterplots of time-averaged ‹q› vs ‹ψ› from 128×128 grid calculations. (a) $T = 0.26$, $t = 41$, Ro $= 7.95 \times 10^{-3}$, $1/\mathrm{Re} = 1.9 \times 10^{-4}$; (b) $T = 0.23$, $t = 61$, Ro $= 7.95 \times 10^{-3}$, $1/\mathrm{Re} = 6 \times 10^{-5}$; (c) $T = 0.25$, $t = 43$, Ro $= 3.18 \times 10^{-3}$, $1/\mathrm{Re} = 6 \times 10^{-5}$; (d) $T = 0.245$, $t = 95$, Ro $= 0.0159$, $1/\mathrm{Re} = 6 \times 10^{-5}$; (e) $T = 0.26$, $t = 37$, Ro $= 1.59 \times 10^{-3}$, $1/\mathrm{Re} = 6 \times 10^{-5}$; (f) $T = 0.25$, $t = 135$, Ro $= 7.95 \times 10^{-3}$, $1/\mathrm{Re} = 1.9 \times 10^{-5}$.
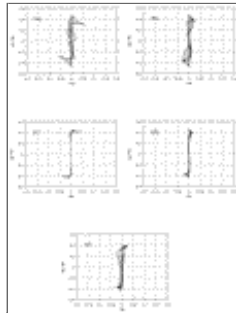
Fig. 16. The viscous development of Fofonoff gyres at $T \sim 0.45$. Scatterplots of time-averaged ‹q› vs ‹ψ› from 128×128 grid calculations. (a) $T = 0.45$, $t = 36$, Ro $= 7.95 \times 10^{-3}$, $1/\mathrm{Re} = 6 \times 10^{-4}$; (b) $T = 0.45$, $t = 49$, Ro $= 7.95 \times 10^{-3}$, $1/\mathrm{Re} = 1.9 \times 10^{-4}$; (c) $T = 0.45$, $t = 42$, Ro $= 1.59 \times 10^{-3}$, $1/\mathrm{Re} = 6 \times 10^{-5}$; (d) $T = 0.46$, $t = 91$, Ro $= 7.95 \times 10^{-3}$, $1/\mathrm{Re} = 6 \times 10^{-5}$; (e) $T = 0.45$, $t = 220$, Ro $= 7.95 \times 10^{-3}$, $1/\mathrm{Re} = 1.9 \times 10^{-5}$.
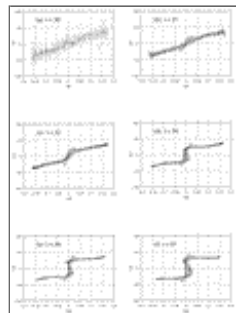
Fig. 17. (a)–(f) The early stages of the time evolution of a Fofonoff gyre due to viscosity; the development and decay of homogenization from $t = 30$ to $t = 41$. Scatterplots of time-averaged ‹q› vs ‹ψ› from 128×128 grid calculations at Ro $= 7.95 \times 10^{-3}$ and $1/\mathrm{Re} = 6 \times 10^{-5}$.
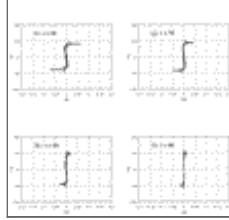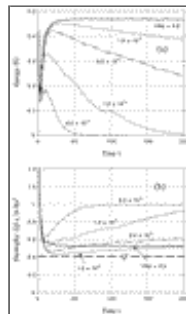
Click on thumbnail for full-sized image.

Fig. 17. (*Continued*) (g)–(l) The late stages of the time evolution of a Fofonoff gyre due to viscosity; the development and decay of homogenization from $t = 46$ to $t = 96$. Scatterplots of time averaged ‹*q*› vs ‹ψ› from 128×128 grid calculations at Ro = 7.95×10^{-3} and $1/Re = 6 \times 10^{-5}$.
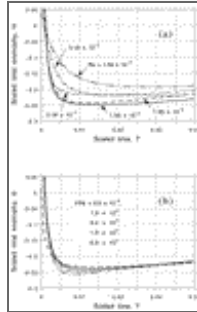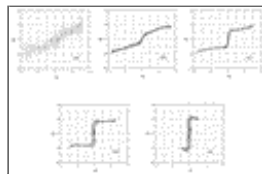

Click on thumbnail for full-sized image.

Fig. 18. The initial stage of the time evolution of the viscous instantaneous (not time-averaged) total potential enstrophy, scaled according to Eq. (7) and computed at grid resolution 128×128, plotted as a function of the scaled time $T = (t - 30)\tau_E/\tau_v$: (a) for different Rossby numbers at $1/Re = 6 \times 10^{-5}$, and (b) for different Reynolds numbers at Ro = 7.95×10^{-3}.

Click on thumbnail for full-sized image.

Fig. 19. The evolution of viscous and inviscid flow starting at $t = 0$ from initial mode 8×8. Time-averaged, domain-integrated energy (a) and potential enstrophy (b) at Ro = 7.95×10^{-3} and grid resolution 128×128, for different Reynolds numbers, plotted as a function of nondimensional time t.

Click on thumbnail for full-sized image.

Fig. 20. Emergence of Fofonoff or homogenized gyres form initial conditions. Scatterplots of time-averaged ‹*q*› vs ‹ψ› at $t = 30$ for the runs shown in Fig. 19 ●▬: (a) $1/Re = 0.0$, (b) 1.9×10^{-6}, (c) 6×10^{-6}, (d) 1.9×10^{-5}, and (e) 6×10^{-5}.

Corresponding author address: Dr. John Dukowicz, Los Alamos National Laboratory, Theoretical Fluid Dynamics, T-3 Mail Stop B216, Los Alamos, NM 87545.

E-mail: duk@lanl.gov